On the Best Settings to Calculate Ionospheric Irregularity Indices From the *In Situ* Plasma Parameters of CSES-01

Michael Pezzopane, Alessio Pignalberi, Paola De Michelis, Giuseppe Consolini, Igino Coco, Fabio Giannattasio, Roberta Tozzi, and Simona Zoffoli

***Abstract*—Electron density (*Ne*) and temperature (*Te*) values recorded by the Langmuir probe onboard the first satellite of the China Seismo-Electromagnetic Satellite (CSES-01) mission allow calculating quantities such as the rate of change of electron density index (RODI) and the rate of change of electron temperature index (ROTEI), which are essential to describe the ionospheric irregularities and their dynamics. These two indices depend significantly on two parameters, i.e., the measurement sampling time and the width of the sliding windows used for their computation. *Ne* and *Te* measurements from CSES-01 present two different sampling times, i.e., 3 s in the survey mode and 1.5 s in the burst mode. The purpose of this article is to understand what are the best values of these two parameters to be used when computing RODI and ROTEI based on CSES-01 data. The main results of the study show the following: The shorter the data sampling time, the higher the values of the calculated ionospheric indices, which means that it is not possible to merge values of either RODI or ROTEI calculated with a different sampling time; the wider the sliding window used to calculate the indices, the higher the indices. A reasonable compromise between the data sampling time and the satellite orbital velocity suggests that the optimal way to calculate RODI and ROTEI from CSES-01 should be done by considering data with a 3-s sampling time (i.e., in the survey mode or in the downsampled burst mode), and a 24-s wide sliding window.**

***Index Terms*—CSES-01 satellite, ionospheric indices, Langmuir probe data, topside ionosphere.**

I. Introduction

THE distribution and dynamics of the topside ionospheric plasma exhibit variations on really different spatial and temporal scales (e.g., [1]–[3]). Specifically, the scale size of ionospheric irregularities ranges from submeters to thousands of kilometers [4], [5]. At large scales, the topside electron density (*Ne*) and temperature (*Te*) behaviors are well described by empirical ionospheric models, like the International Reference Ionosphere (IRI; [6]). Instead, at small scales, the *Ne* and *Te* behaviors can be investigated through the calculation of specific indices based on *in situ* observations from instruments onboard low-Earth-orbit satellites, such as the rate of change of electron density index (RODI; [7]) and the rate of change of electron temperature index (ROTEI; [8], [9]). These two indices allow identifying a large spectrum of irregularities, which characterize both the high latitudes (e.g., [10]–[13]) and the low latitudes (e.g., [14]–[16]).

The *in situ* measurements performed by the Langmuir probe (LAP) onboard CSES-01, the first satellite of the China Seismo-Electromagnetic Satellite (CSES, also called ZhangHeng-1, ZH-1) mission [17], are considered with two different sampling times, i.e., 3 s in the survey mode and 1.5 s in the burst mode. As we were willing to calculate ionospheric indices from CSES data, the following questions arose: How a different sampling time affects them? More specifically, can indices computed in burst and survey modes be merged? How do they depend on the width of the sliding window used in their computation? The present study aims at answering all these questions. Concerning the last one, it is well known that the width of the sliding window is a crucial parameter for the detection of fluctuations on different spatial and temporal scales. When the sampling time is either 1 s or 0.5 s, as is the case of the Swarm mission [18], a good compromise is to select a 10-s wide sliding time window, as was done, for instance, in [7], [13], and [19]. However, CSES-01 presents longer sampling times, which prompted us to do a more in-depth study to understand what is the optimal sliding time window width to calculate both RODI and ROTEI starting from CSES-01 data. CSES-01 LAP *Ne* and *Te* measurements were recently compared to those recorded by Swarm and DEMETER satellites, the Millstone Hill incoherent scatter radar, and values modeled by the IRI empirical model [20]–[22]. Overall, these preliminary comparisons identified some differences in the *Ne* and *Te* magnitude among the different datasets, but their quite similar spatial and seasonal patterns make CSES-01 data very promising for ionospheric studies.

Manuscript received January 19, 2022; revised April 4, 2022 and April 19, 2022; accepted April 22, 2022. Date of publication April 26, 2022; date of current version May 30, 2022. This work was supported by the Italian Space Agency (ASI) in the Framework of Contract ASI "LIMADOU Scienza+" no. 2020-31-HH.0. *(Corresponding author: Michael Pezzopane.)*

Michael Pezzopane, Alessio Pignalberi, Paola De Michelis, Igino Coco, Fabio Giannattasio, and Roberta Tozzi are with the Istituto Nazionale di Geofisica e Vulcanologia, 00143 Rome, Italy (e-mail: michael.pezzopane@ingv.it; alessio.pignalberi@ingv.it; paola.demichelis@ingv.it; igino.coco@ingv.it; fabio.giannattasio@ingv.it; roberta.tozzi@ingv.it).

Giuseppe Consolini is with the Istituto Nazionale di Astrofisica-Istituto di Astrofisica e Planetologia Spaziali, 00133 Rome, Italy (e-mail: giuseppe.consolini@inaf.it).

Simona Zoffoli is with the Agenzia Spaziale Italiana, 00133 Rome, Italy (e-mail: simona.zoffoli@asi.it).

This article has supplementary downloadable material available at https://doi.org/10.1109/JSTARS.2022.3170339, provided by the authors.

Digital Object Identifier 10.1109/JSTARS.2022.3170339

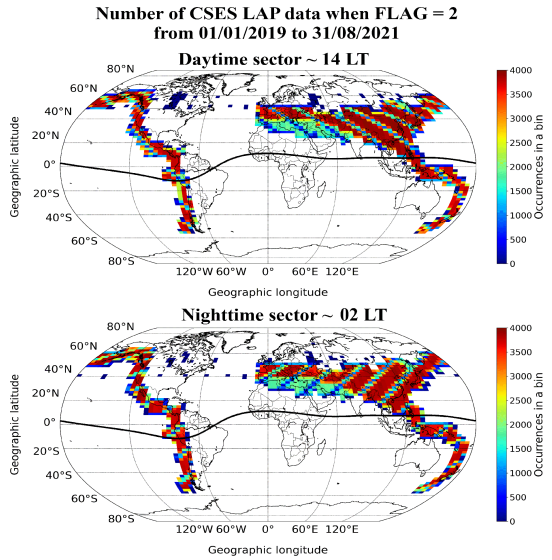

Fig. 1. CSES-01 LAP data recorded in the burst mode (FLAG = 2) from January 1, 2019 to August 31, 2021, and plotted in geographic coordinates. The color scale represents the number of measurements in each bin (bins are 2° wide in latitude and 4° wide in longitude). The top panel is for the daytime sector (~14 LT) and the bottom panel is for the nighttime sector (~02 LT). The black curve in both panels represents the geomagnetic equator.

Section II will describe the data and methods used. Section III will describe how different sampling times affect the computed ionospheric indices, whereas Section IV will describe how different sliding time window widths affect the computed ionospheric indices. The summary and conclusions are the subjects of Section V.

II. Data and Methods

CSES-01 is a Sun-synchronous satellite flying with an orbital inclination of 97.4°, an altitude of ~500 km, and descending and ascending nodes are at ~14 local time (LT) and ~02 LT, respectively. The main scientific objective of the CSES mission is to get data on the ionospheric environment to monitor and study perturbations possibly associated with earthquake activity [17]. Anyway, its payload is valuable to perform wider studies linked to the topside ionosphere. In this work, *N*e and *T*e data measured by LAP [23], [24] from January 1, 2019, to August 31, 2021, have been considered. These consist of Level-2 calibrated data with a sampling time of 3 s in the survey mode (identified as FLAG = 1) and a sampling time of 1.5 s in the burst mode (identified as FLAG = 2), the latter being available only for definite regions of the terrestrial globe (see Fig. 1). CSES-01 data are recorded only in a geographical latitudinal range mainly between 70°S and 70°N, so they are not representative of high latitudes.

RODI values can be derived from *N*e measurements by applying the procedure described in [8]. As a first step, the rate of change of electron density (ROD) is calculated as the time derivative of *N*e along the satellite's orbit. *N*e values are continuous time series for a specific semiorbit, with a defined sampling time (survey or burst mode depending on the location). By indexing with k the contiguous measured values recorded at different times t_k, the kth ROD value is calculated as follows:

$$\mathrm{ROD}_k = \frac{Ne_{k+1} - Ne_k}{t_{k+1} - t_k} \tag{1}$$

where Ne_k is the electron density measured at time t_k. In order to exclude the effect of possible gaps in *N*e data, ROD values are calculated only for time-consecutive measurements, i.e., when the condition $(t_{k+1} - t_k) = \Delta t = 3$ s (or 1.5 s) is met.

The second step consists of organizing the calculated ROD values in windows of width ΔT centered at time t_k, sliding along the satellite's orbit. For each window, the arithmetic mean of ROD at time t_k is calculated by considering all the values falling inside the window and then between $(t_k - \Delta T/2)$ and $(t_k + \Delta T/2)$

$$\overline{\mathrm{ROD}}_k = \frac{1}{N}\sum_{i=-j}^{j} \mathrm{ROD}_{k+i} \tag{2}$$

where ROD_{k+i} are ROD values falling inside the rectangular window of width ΔT centered at time t_k and containing $N = 2j + 1$ values.

Finally, the RODI value at time t_k is calculated as the standard deviation of the ROD values inside the window

$$\mathrm{RODI}_k = \sqrt{\frac{1}{N-1}\sum_{i=-j}^{j}\left(\mathrm{ROD}_{k+i} - \overline{\mathrm{ROD}}_k\right)^2}. \tag{3}$$

RODI is calculated only when at least half of the maximum number of occurrences that could fall in a window are actually present; otherwise, the window sample is considered not statistically significant and discarded. For example, if $\Delta T = 30$ s and $\Delta t = 3$ s (survey mode), at most 11 ROD values fall in the window and at least 6 ROD values are needed for the RODI calculation.

Recently, in [8], the ROTEI index is introduced by applying the same mathematical approach to *T*e values. As a consequence, ROTEI is defined as the standard deviation of the rate of change of electron temperature (ROTE) values inside a window sliding along the satellite's orbit and is calculated by applying (1)–(3) to *T*e values. Specifically

$$\mathrm{ROTE}_k = \frac{Te_{k+1} - Te_k}{t_{k+1} - t_k} \tag{4}$$

where Te_k is the electron temperature measured at time t_k and

$$\overline{\mathrm{ROTE}}_k = \frac{1}{N}\sum_{i=-j}^{j} \mathrm{ROTE}_{k+i} \tag{5}$$

where ROTE_{k+i} are ROTE values falling inside a window of width ΔT centered at t_k and containing $N = 2j + 1$ values. Finally, the ROTEI value at time t_k is calculated as the standard deviation of the ROTE values inside the window

$$\mathrm{ROTEI}_k = \sqrt{\frac{1}{N-1}\sum_{i=-j}^{j}\left(\mathrm{ROTE}_{k+i} - \overline{\mathrm{ROTE}}_k\right)^2}. \tag{6}$$

Since the width of the window is crucial for detecting fluctuations of different spatial and temporal scales, in the next sections,

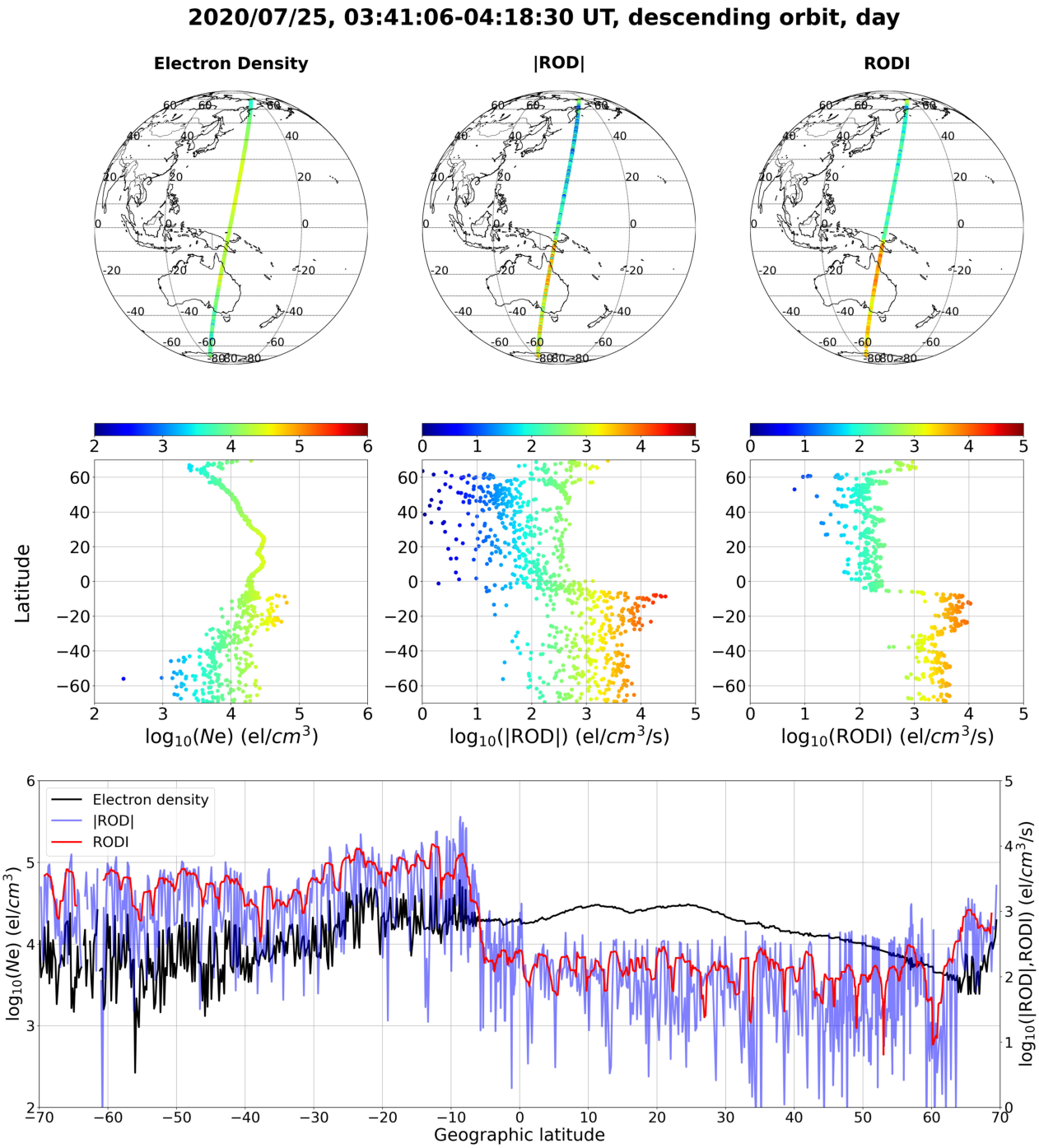

Fig. 2. Electron density (left column), |ROD| (where ROD is calculated through (1), middle column), and RODI (right column) values recorded by CSES-01 on July 25, 2020, between 03:41 UT and 04:18 UT, for a descending orbit in the daytime sector (∼14 LT). Data are represented in geographic maps (top row) and as separated (middle row) and superposed (bottom row) time series. In the top and middle rows, data are represented as scatter points whose color identifies the corresponding magnitude (in logarithmic scale). In the bottom row, data are represented as curves of different colors: black for *N*e, light blue for |ROD|, and red for RODI.

we will investigate the use of windows with different ΔT values, i.e., encompassing a different number of ROD and ROTE values.

Examples of RODI and ROTEI indices obtained from CSES-01 LAP observations recorded on July 25, 2020, during the main phase of a weak geomagnetic storm with a minimum Dst equal to −75 nT and a maximum Kp equal to 4, for a descending orbit in the daytime sector (∼14 LT), are reported in Figs. 2 and 3. In these cases, both indices were calculated with $\Delta T = 24$ s and $\Delta t = 3$ s. These figures clearly display the ability of both indices in catching small-scale variations in *N*e and *T*e, respectively. In fact, between about 5°S and 70°S, large variations in the magnitude of both *N*e and *T*e cause steep increases in both RODI and ROTEI (the scale is logarithmic). Due to their mathematical definition, RODI and ROTEI describe the variability of *N*e and

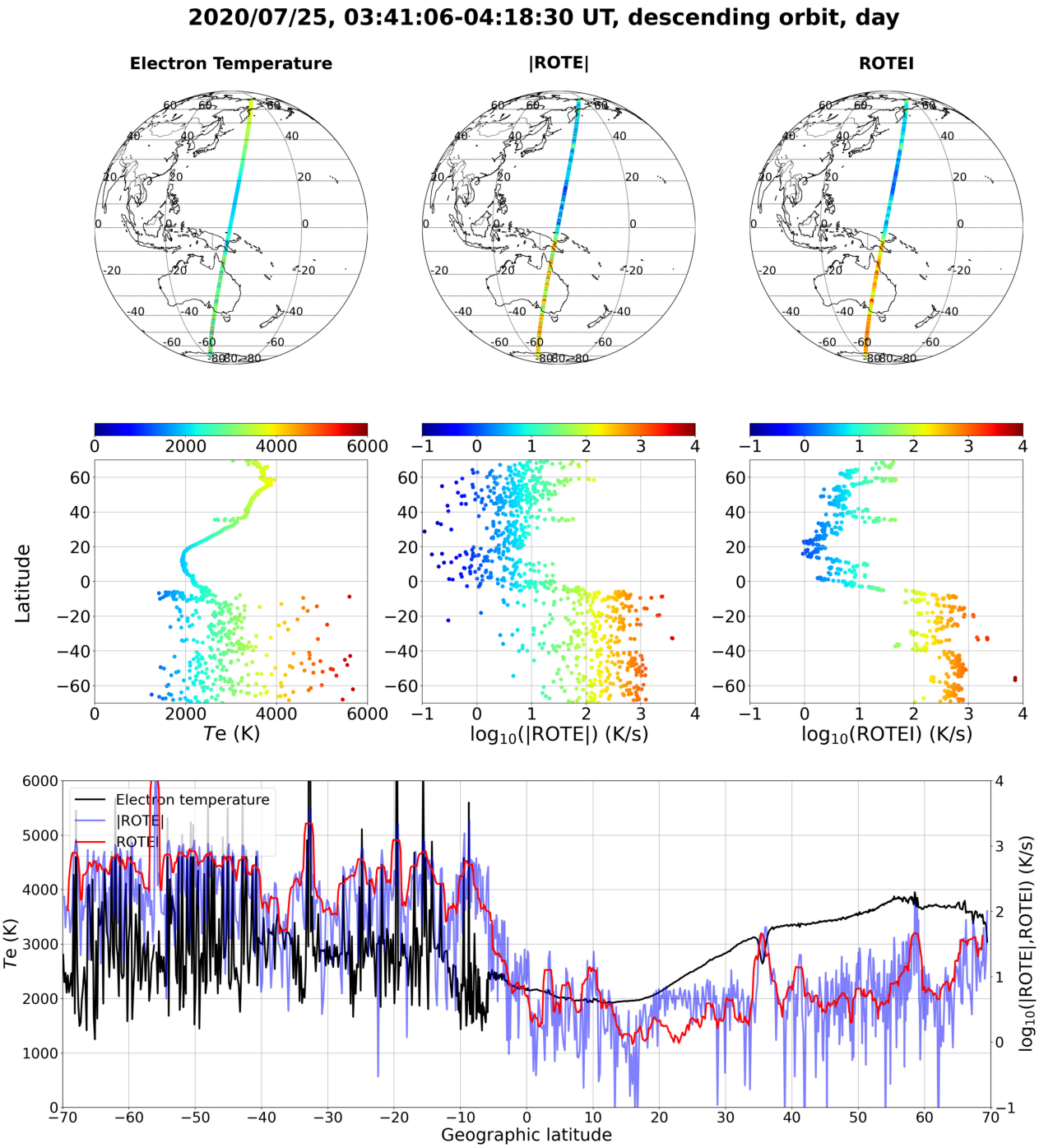

Fig. 3. Electron temperature (left column), |ROTE| (where ROTE is calculated through (4), middle column), and ROTEI (right column) values recorded by CSES-01 on July 25, 2020, between 03:41 UT and 04:18 UT, for a descending orbit in the daytime sector (∼14 LT). Data are represented in geographic maps (top row) and as separated (middle row) and superposed (bottom row) time series. In the top and middle rows, data are represented as scatter points whose color identifies the corresponding magnitude (in logarithmic scale). In the bottom row, data are represented as curves of different colors: black for *Te*, light blue for |ROTE|, and red for ROTEI.

Te at the scale of the window used for their calculation and are unaffected by large-scale variations. This is well visible in Figs. 2 and 3 by comparing the smooth trend characterizing the Northern hemisphere with the oscillating one characterizing the Southern hemisphere, which results in a difference of more than two orders of magnitude between the lowest and the highest values of RODI and ROTEI.

III. Effect of Different CSES-01 LAP Sampling Times on the Ionospheric Index Calculation

By definition, the magnitude of both RODI and ROTEI depends on the observation sampling time Δt. To investigate the effect of different CSES-01 LAP sampling times, we here consider only data acquired in the burst mode (with a sampling time of 1.5 s) but use it to build a further dataset

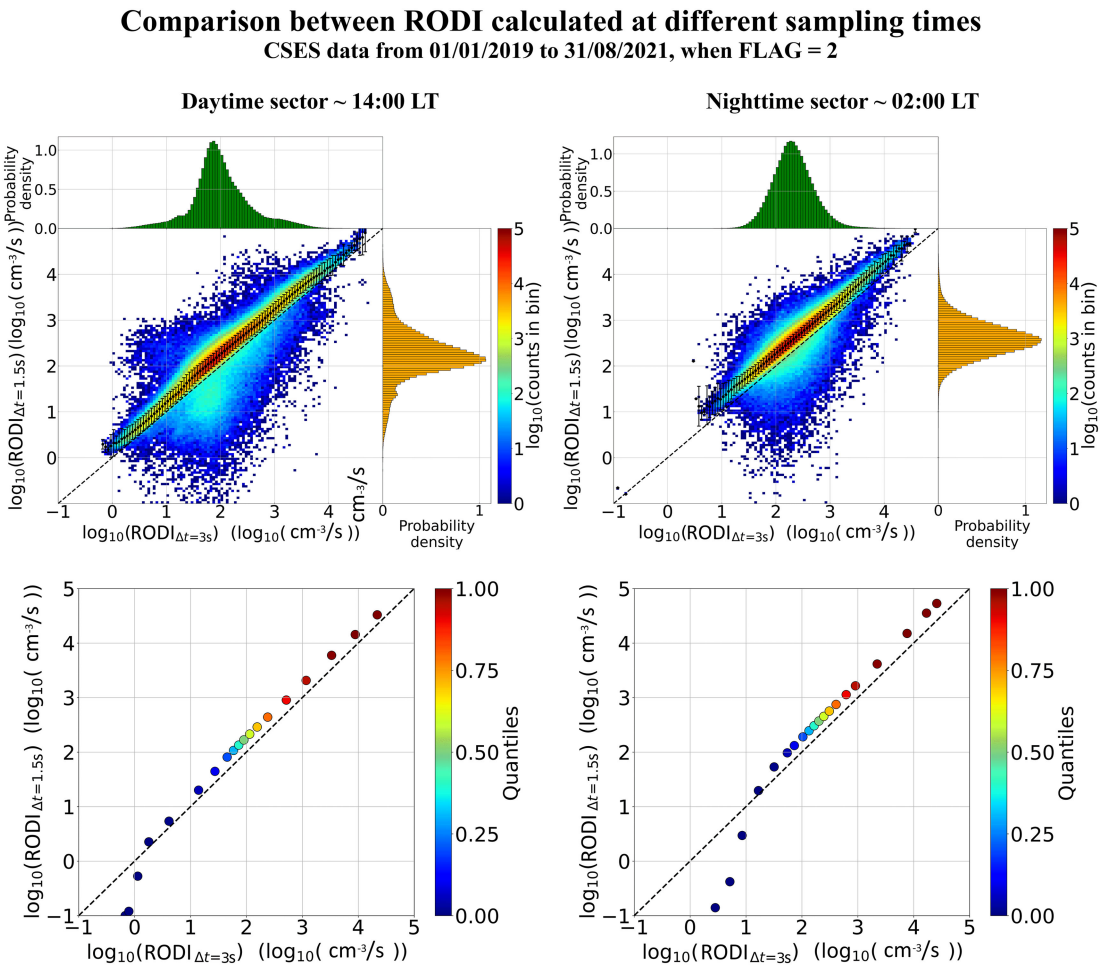

Fig. 4. (Top panels) Joint probability distribution of RODI values calculated with different sampling times: $\text{RODI}_{\Delta t=3\text{s}}$ on the x-axis, $\text{RODI}_{\Delta t=1.5\text{s}}$ on the y-axis. Black dots with error bars represent the mean and standard deviation of $\text{RODI}_{\Delta t=1.5\text{s}}$ conditioned by $\text{RODI}_{\Delta t=3\text{s}}$. CSES-01 data are those recorded from January 1, 2019, to August 31, 2021, in those regions where LAP measured in the burst mode (see Fig. 1). On the top and right of the distributions, histograms of the probability density for $\text{RODI}_{\Delta t=3\text{s}}$ and $\text{RODI}_{\Delta t=1.5\text{s}}$ are also reported. (Bottom panels) Q–Q plots between $\text{RODI}_{\Delta t=3\text{s}}$ and $\text{RODI}_{\Delta t=1.5\text{s}}$. The values of quantiles of both distributions are represented in color scale. The dashed lines represent the bisector of the first-third quadrant. Left panels refer to the daytime sector, whereas right panels refer to the nighttime sector. The considered window width is $\Delta T = 30$ s.

made of data characterized by a 3-s sampling time (obtained by downsampling the 1.5-s time series). Since, usually, both *Ne* and *Te* exhibit variations at time scales lower than those probed by CSES-01 LAP, the two different sampling times produce different ROD and ROTE values [through (1) and (4), respectively] and, consequently, also different RODI and ROTEI.

To test the effect of different sampling times on the index values, with a sliding window of fixed width, we selected the CSES-01 dataset measured in the burst mode and calculated RODI and ROTEI values with the following two specifications:

1) $\text{RODI}_{\Delta t=3\text{s}}$ and $\text{ROTEI}_{\Delta t=3\text{s}}$, i.e., RODI and ROTEI values obtained with $\Delta t = 3$ s and $\Delta T = 30$ s, and at most $N = 11$ values in the sliding window;
2) $\text{RODI}_{\Delta t=1.5\text{s}}$ and $\text{ROTEI}_{\Delta t=1.5\text{s}}$, i.e., RODI and ROTEI values obtained with $\Delta t = 1.5$ s and $\Delta T = 30$ s, and at most $N = 21$ values in the sliding window.

Fig. 4 shows the comparison between RODI values calculated according to the two aforementioned settings. The comparison is performed through the graphical representation of joint probability distributions and quantile–quantile (Q–Q) plots of $\text{RODI}_{\Delta t=3\text{s}}$ and $\text{RODI}_{\Delta t=1.5\text{s}}$ values, for the two different LT sectors probed by CSES-01. In the joint probability distribution plots, the mean and standard deviation of $\text{RODI}_{\Delta t=1.5\text{s}}$ conditioned by $\text{RODI}_{\Delta t=3\text{s}}$ are also reported as black points and vertical bars, respectively. By looking at joint probability distribution plots, it is clear how $\text{RODI}_{\Delta t=1.5\text{s}} > \text{RODI}_{\Delta t=3\text{s}}$ for the bulk of dataset, with conditioned mean values above the bisector of the first-third quadrant (dashed line) in the entire range of calculated RODI values. The Q–Q plot is a scatterplot of two sets of quantiles that gives information on the similarity between the two distributions of data [25]. In fact, if both sets of quantiles came from the same distribution, they will distribute along a straight line. Fig. 4 shows that quantiles distribute along a straight line only above a certain RODI threshold value, whereas lower quantiles (those associated with the tail of the distribution concerning the lowest RODI values) depart from this behavior. As a consequence, the two distributions of $\text{RODI}_{\Delta t=3\text{s}}$ and $\text{RODI}_{\Delta t=1.5\text{s}}$ values can be considered quite similar, with

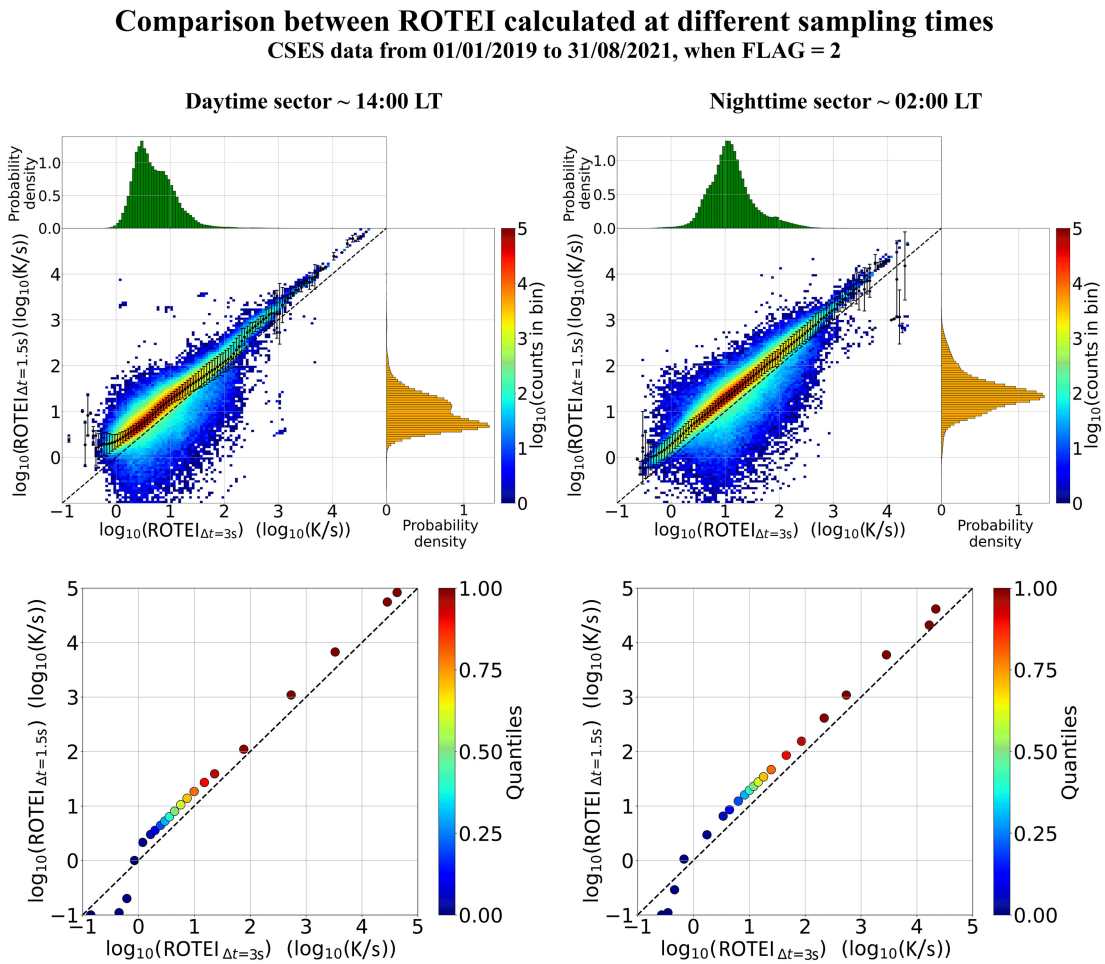

Fig. 5. (Top panels) Joint probability distribution of ROTEI values calculated with different sampling times: $\text{ROTEI}_{\Delta t=3\text{s}}$ on the x-axis, $\text{ROTEI}_{\Delta t=1.5\text{s}}$ on the y-axis. Black dots with error bars represent the mean and standard deviation of $\text{ROTEI}_{\Delta t=1.5\text{s}}$ conditioned by $\text{ROTEI}_{\Delta t=3\text{s}}$. CSES-01 data are those recorded from January 1, 2019 to August 31, 2021, in those regions where LAP measured in the burst mode (see Fig. 1). On the top and right of the distributions, histograms of the probability density for $\text{ROTEI}_{\Delta t=3\text{s}}$ and $\text{ROTEI}_{\Delta t=1.5\text{s}}$ are also reported. (Bottom panels) Q–Q plots between $\text{ROTEI}_{\Delta t=3\text{s}}$ and $\text{ROTEI}_{\Delta t=1.5\text{s}}$. The values of quantiles of both distributions are represented in color scale. The dashed lines represent the bisector of the first-third quadrant. Left panels refer to the daytime sector, whereas right panels refer to the nighttime sector. The considered window width is $\Delta T = 30$ s.

differences only at the tail of the lowest RODI values. Moreover, most of the $\text{RODI}_{\Delta t=1.5\text{s}}$ quantiles are higher than $\text{RODI}_{\Delta t=3\text{s}}$ ones (they are above the bisector of the first-third quadrant), as already highlighted by the joint probability distribution plots. To sum up, the shorter the data sampling time, the higher the calculated RODI values, with the corresponding distributions being very similar except for the very low quantiles, which are related to low RODI values that are few and those we are least interested in.

Fig. 5 shows the same analysis as in Fig. 4 but for ROTEI. Corresponding results are very similar to those obtained for RODI and confirm that the shorter the data sampling time, the higher the calculated ionospheric index values. This result is similar to that found by Li *et al.* [26] in their analyses finalized to look for seismological ionospheric signatures. This means that both *Ne* and *Te* exhibit variability at time scales smaller than those probed by CSES-01 LAP.

The results of this analysis highlight that it is not possible to merge values of RODI or ROTEI calculated with different sampling times because their magnitude is sensibly different. This is highlighted also in Fig. 6, which is an example of median daytime RODI values, with both a sampling time of 1.5 s and a sampling time of 3 s (obtained by downsampling the 1.5-s time series), calculated only in the region where the satellite records in the burst mode. As a consequence, in the following analyses, RODI and ROTEI will be calculated with a fixed sampling time $\Delta t = 3$ s. In this way, RODI and ROTEI values obtained in both survey and burst modes are comparable and the entire CSES dataset (both FLAGS) can be used.

IV. Effect of Different Time Window Widths on the Ionospheric Index Calculation

To investigate the effect that the width ΔT of the sliding window has on the index magnitude, we calculated RODI and ROTEI by using windows of different widths and fixing the sampling time to $\Delta t = 3$ s, for the entire CSES-01 LAP dataset.

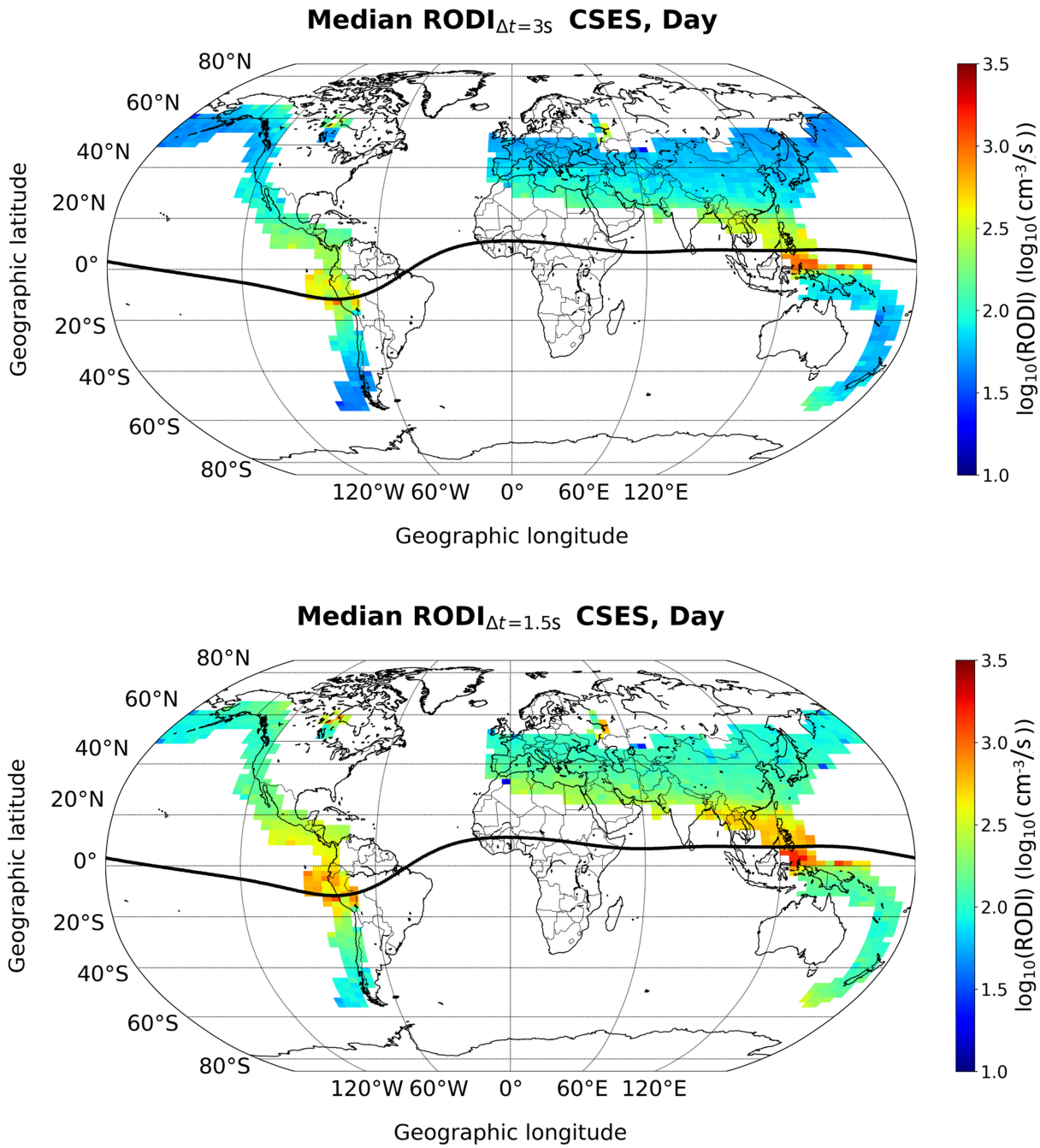

Fig. 6. Median RODI calculated from January 1, 2019 to August 31, 2021, for the daytime sector (∼14 LT) in the regions where CSES-01 LAP data have been recorded in the burst mode (FLAG = 2) and plotted in geographic coordinates. The top panel refers to a sampling time of 3 s (obtained by downsampling the 1.5-s time series), whereas the bottom panel refers to a sampling time of 1.5 s. Bins are 2° wide in latitude and 4° wide in longitude. The black curve in both panels represents the geomagnetic equator. The figure for the nighttime sector can be found in the Supplementary Material.

This means that we considered all survey mode data and burst mode data downsampled at 3 s.

Specifically, we tested seven windows of width $\Delta T = [12, 18, 24, 30, 36, 42, \text{and } 48]$ s. Then, seven RODI and ROTEI datasets were obtained. To compare them, we applied the same analysis shown in Figs. 4 and 5 by putting the dataset obtained with $\Delta T = 30$ s on the x-axis and the ones obtained with different ΔT values on the y-axis. This means that the differences among RODI and ROTEI values obtained with different ΔT values are evaluated by taking $\Delta T = 30$ s as a touchstone. Corresponding comparisons are shown in Figs. 7–10 for both RODI and ROTEI, for the daytime sector. The corresponding analyses related to the nighttime sector can be found in the Supplementary Material.

Figs. 7–10 highlight the effect that the use of windows of different widths has on the index calculation. In fact, as it is well testified by the data distribution compared to the bisector of the first-third quadrant in the joint probability distribution

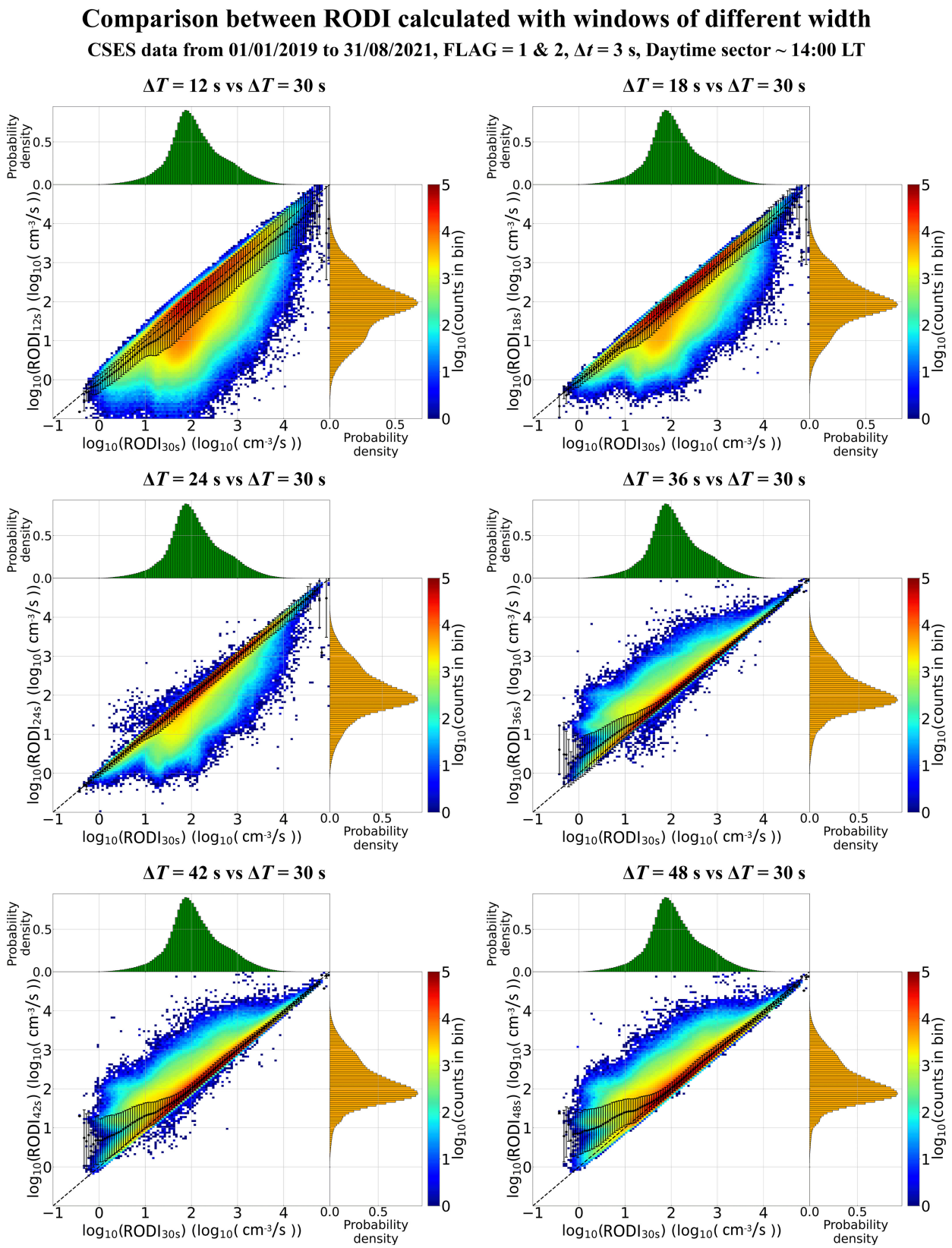

Fig. 7. Joint probability distribution of RODI values calculated with the sampling time fixed to $\Delta t = 3$ s. In each of the six panels, the RODI dataset calculated with $\Delta T = 30$ s ($\text{RODI}_{30\text{s}}$) is reported on the x-axis, whereas RODI datasets for different ΔT values are reported on the y-axis. CSES-01 LAP data are those recorded from January 1, 2019, to August 31, 2021, for the daytime sector.

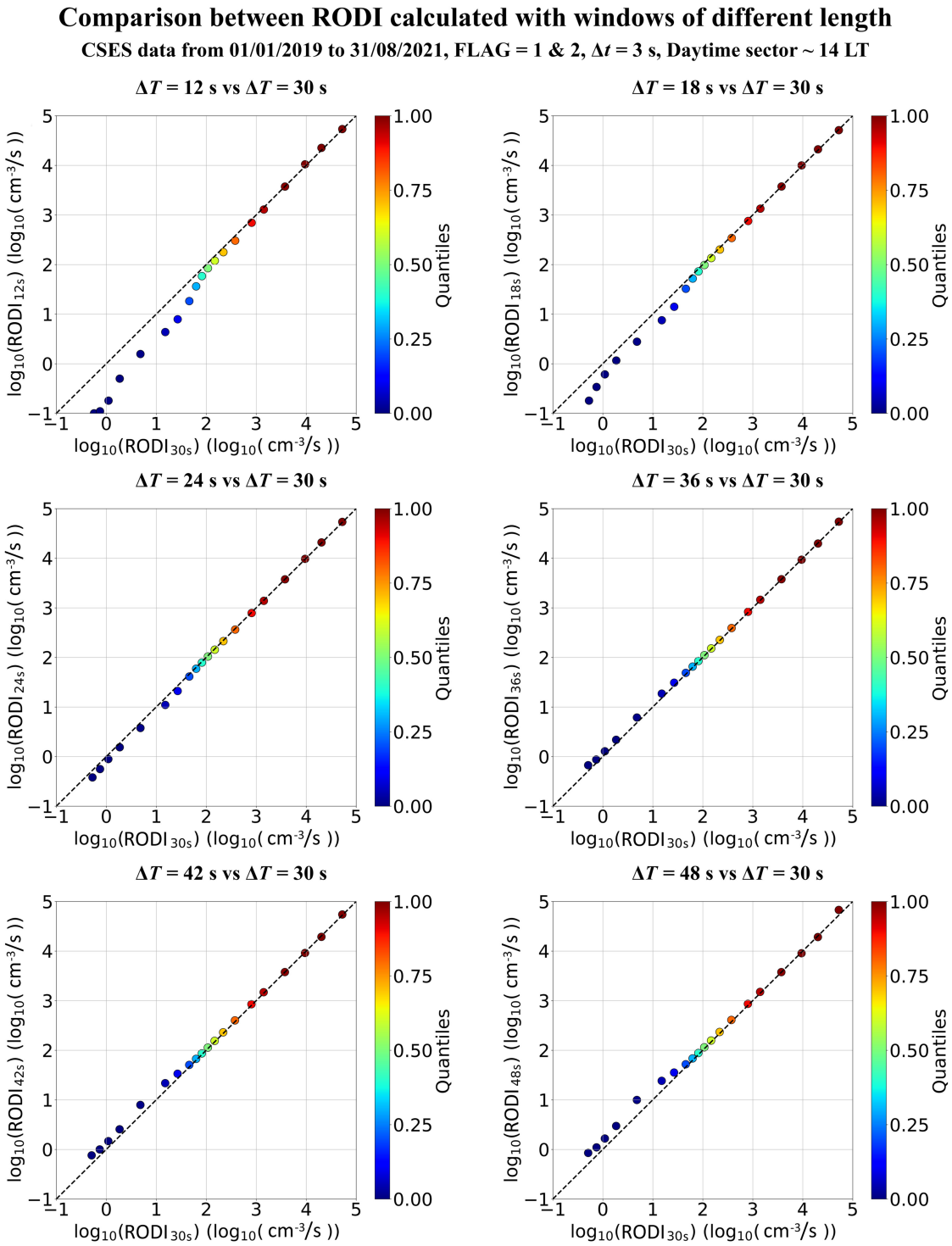

Fig. 8. Q–Q plots of RODI values calculated with the sampling time fixed to $\Delta t = 3$ s. In each of the six panels, the RODI dataset calculated with $\Delta T = 30$ s ($\text{RODI}_{30\text{s}}$) is reported on the x-axis, whereas RODI datasets for different ΔT values are reported on the y-axis. CSES-01 LAP data are those recorded from January 1, 2019, to August 31, 2021, for the daytime sector.

plots, the wider the window, the higher the calculated indices. When $\Delta T < 30$ s, a portion of data distribute below the bisector of the first-third quadrant, which means that $\text{RODI}_{[12,18,24]\text{s}} < \text{RODI}_{30\text{s}}$; the reverse is true when $\Delta T > 30$ s (which means that $\text{RODI}_{[36,42,48]\text{s}} > \text{RODI}_{30\text{s}}$). A similar behavior holds also for ROTEI. By looking at Q–Q plots, we can see that the effect of the window width change is clear above all at the tails of the distributions. Overall, slight differences are visible for the ranges $\Delta T \in [24, 36]$ s, so the three options (24, 30, and 36 s) can be considered rather equivalent. Instead, a further decrease or increase in the window width produces larger differences above all at the tails of the distributions. CSES-01 satellite moves at

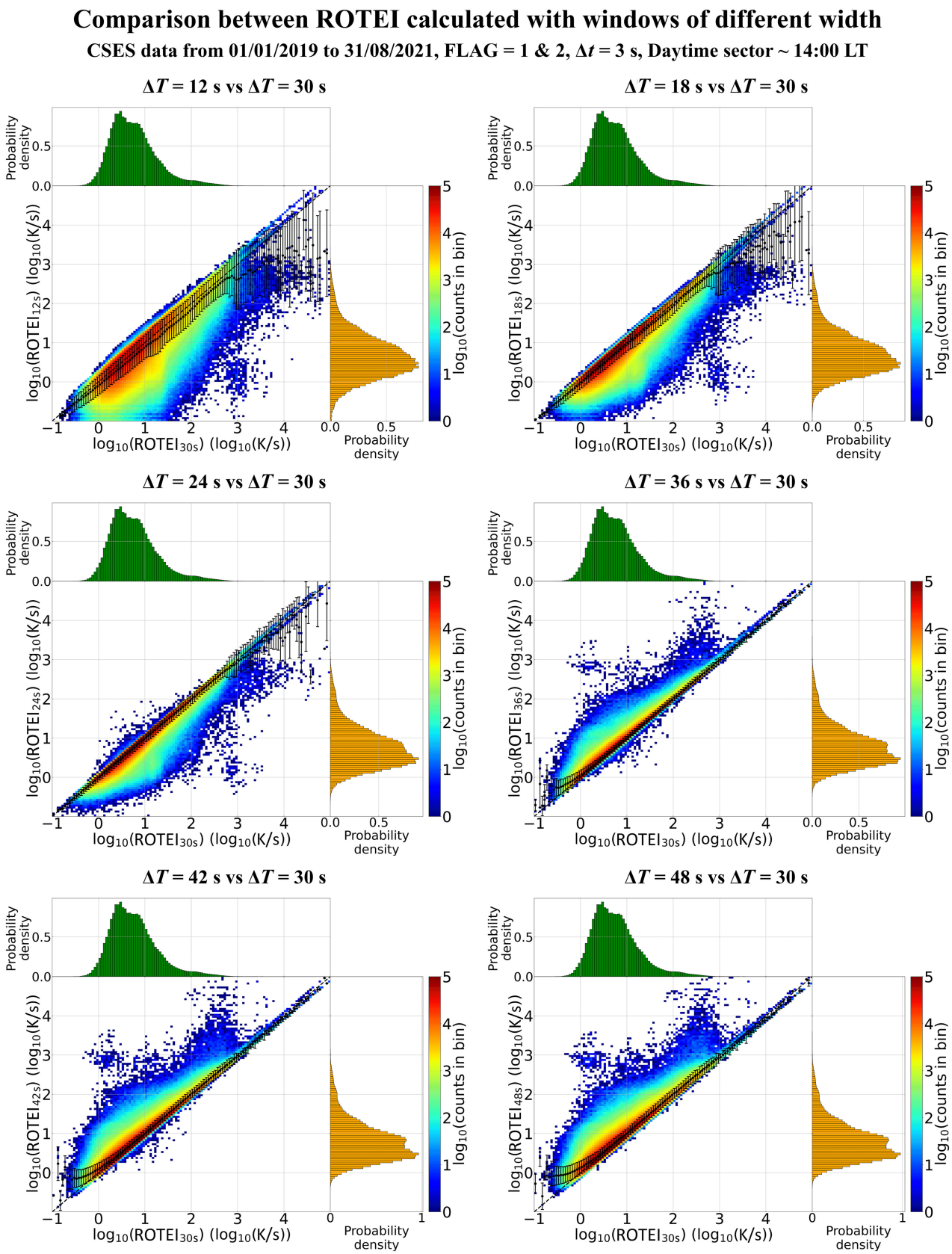

Fig. 9. Joint probability distribution of ROTEI values calculated with the sampling time fixed to $\Delta t = 3$ s. In each of the six panels, the ROTEI dataset calculated with $\Delta T = 30$ s ($\text{ROTEI}_{30\text{s}}$) is reported on the x-axis, whereas ROTEI datasets for different ΔT values are reported on the y-axis. CSES-01 LAP data are those recorded from January 1, 2019 to August 31, 2021, for the daytime sector.

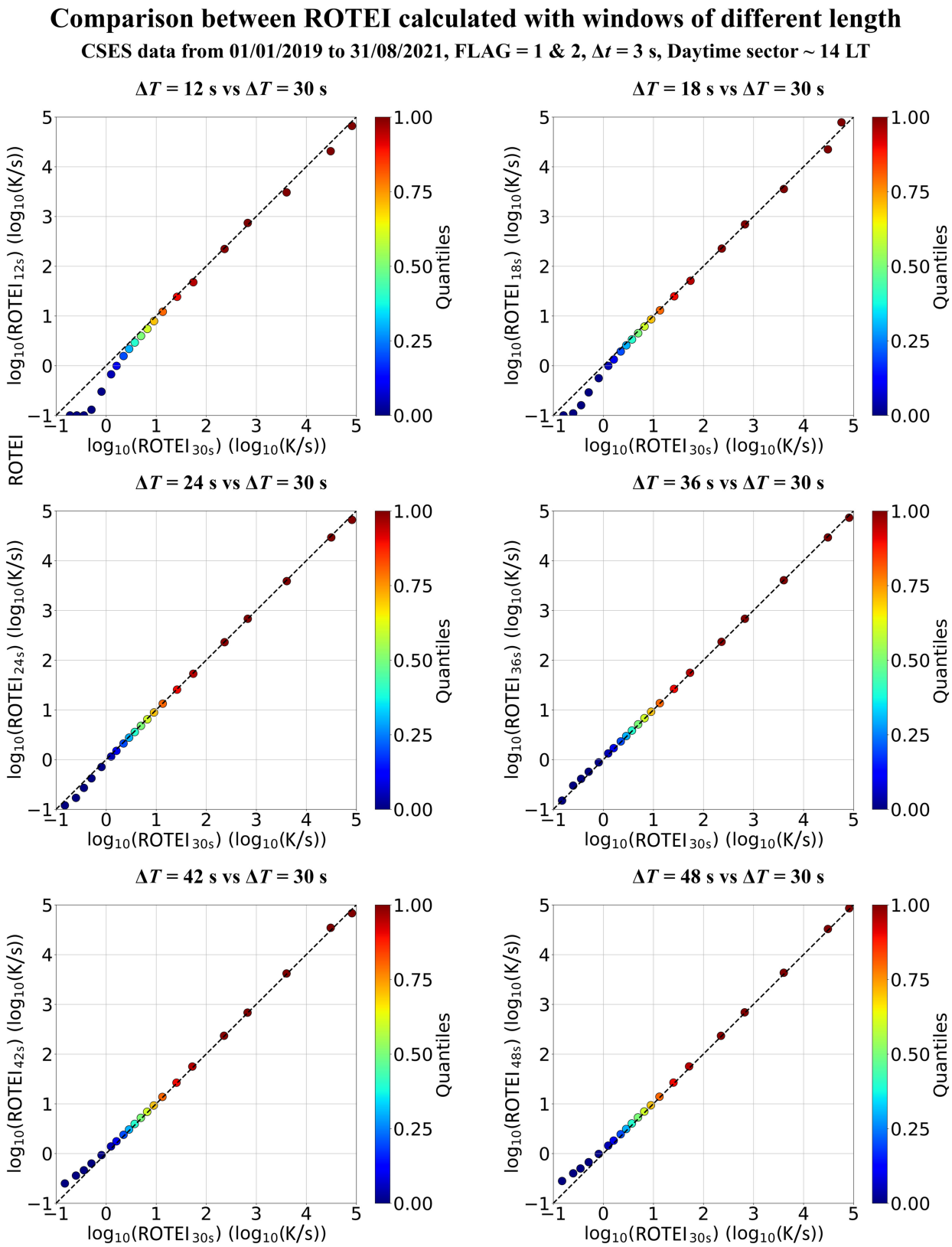

Fig. 10. Q–Q plots of ROTEI values calculated with the sampling time fixed to $\Delta t = 3$ s. In each of the six panels, the ROTEI dataset calculated with $\Delta T = 30$ s ($\text{ROTEI}_{30\text{s}}$) is reported on the x-axis, whereas ROTEI datasets for different ΔT values are reported on the y-axis. CSES-01 LAP data are those recorded from January 1, 2019 to August 31, 2021, for the daytime sector.

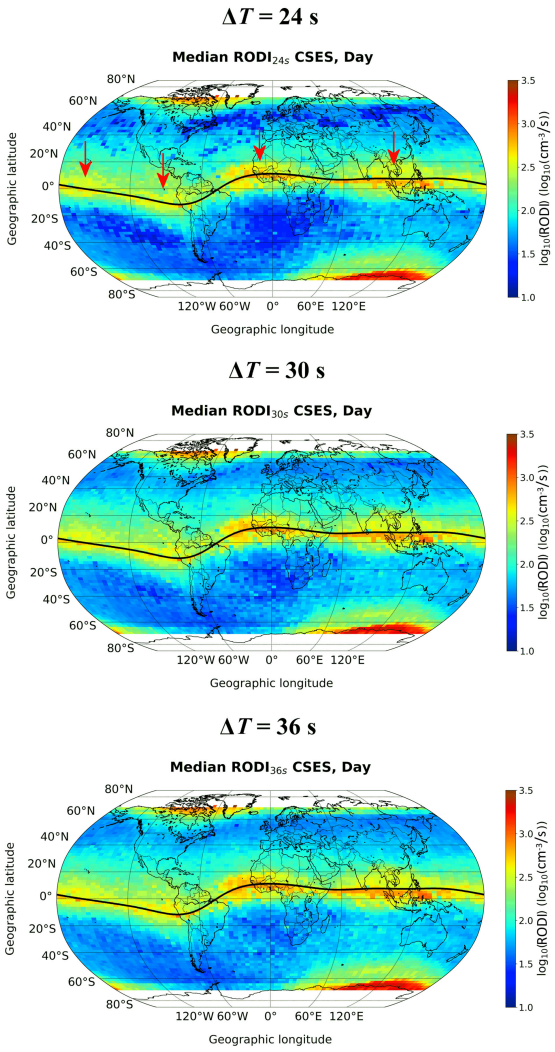

Fig. 11. Median RODI calculated from January 1, 2019 to August 31, 2021for the daytime sector (∼14 LT) with $\Delta t = 3$ s, for $\Delta T = 24$ s (top panel), $\Delta T = 30$ s (middle panel), and $\Delta T = 36$ s (bottom panel), plotted in geographic coordinates. Bins are 2° wide in latitude and 4° wide in longitude. In the top panel, four red arrows highlight the position of four maxima that are well visible also in the middle and bottom panels. The black curve in all the panels represents the geomagnetic equator. The figure for the nighttime sector can be found in the Supplementary Material.

about 7.5–8.0 km/s, and then data are taken in different spatial regions. Consequently, the time and spatial scales are tied by the satellite velocity, and to study the local small-scale properties of both *N*e and *T*e, we would need a window as short as possible. At the same time, however, the choice of the window width is affected by both the measurement sampling time and the need of having enough data in the window, in order to obtain an index statistically significant.

Finally, we need to find a reasonable compromise according to both the data sampling time and the satellite orbital velocity. This is why we think that the best choice is to set ΔT to 24 s. This choice is supported also by what is shown in Fig. 11, which is an example of median daytime RODI values, for $\Delta t = 3$ s and $\Delta T \in [24, 36]$ s. The three maps show similar large-scale patterns. For instance, at low latitudes, four maxima can be observed in the longitudinal variation of electron density. These features were first discovered by Immel *et al.* [27] in IMAGE/EUV observations, then confirmed by Lühr *et al.* [28] with CHAMP data, and by Scherliess *et al.* [29] with TOPEX data. Moreover, part of the auroral boundaries in both hemispheres can be seen, in agreement with recent works by Jin *et al.* [7] and Pezzopane *et al.* [19]. Although the choice of the window width in the range [24, 36] s seems not to dramatically affect the climatological maps of RODI, the shortest window is the most indicated to highlight small-scale patterns, which emerge by looking at individual orbits. With this choice, the maximum number of data points included in the sliding window will be 9 in the survey mode ($\Delta t = 3$ s) and 17 in the burst mode ($\Delta t = 1.5$ s). Considering the satellite orbital velocity with $\Delta T = 24$ s, we are considering data collected in a 180–192 km wide region.

V. Summary and Conclusion

The main goal of the CSES mission is to look for ionospheric perturbations possibly associated with earthquakes. To this end, the calculation of indices, such as RODI and ROTEI, could be valid help. In this article, we have investigated the effects of different sampling times and different sliding window widths when calculating RODI and ROTEI based on *N*e and *T*e measurements made by LAP onboard CSES-01 satellite. Considering that these two indices are essential to describe the ionospheric irregularities and dynamics, it is easy to understand the importance of the choice of these two parameters. To accomplish this task, we have considered *N*e and *T*e measurements recorded between January 1, 2019 to August 31, 2021 in both survey (sampling time of 3 s) and burst (sampling time of 1.5 s) modes. The main outcomes of the study can be summarized as follows.

1) It is not possible to merge values of RODI or ROTEI calculated with different sampling times because their magnitude is sensibly different; the shorter the data sampling time, the higher the calculated indices. By taking into account that CSES-01 LAP data are recorded in the burst mode ($\Delta t = 1.5$ s) only for a limited portion of the Earth's surface, we suggest calculating RODI and ROTEI considering a sampling time of 3 s. In this way, the whole CSES dataset can be used;
2) The wider the sliding window used to calculate the indices, the higher the indices. Anyhow, to study the small-scale properties of both *N*e and *T*e, the window cannot be too wide, but at the same time, it must contain a number of points, such as to obtain a statistically significant index. According to the analyses shown in this article, we suggest setting the width of the sliding window to 24 s.

The results of this study represent the first fundamental step toward the implementation of a standard procedure to calculate RODI and ROTEI from CSES-01 satellite LAP data. In order to characterize the small-scale irregularities of the topside ionosphere, which is crucial for space weather purposes, it is the intention of the authors to explore in the near future the main spatial, seasonal, and solar activity variations exhibited by these indices, calculated through the procedure outlined in this work, and compare them with those based on Swarm data.

ACKNOWLEDGMENT

This work has been done in the framework of the CSES-LIMADOU collaboration.[1] This work made use of the data from CSES mission, a project funded by the China National Space Administration and the China Earthquake Administration in collaboration with the Italian Space Agency and the Istituto Nazionale di Fisica Nucleare. CSES-01 data are freely available at[2] under request. The authors acknowledge the CSES mission data providers for the significant investments of their time, effort, expertise, and funds needed to acquire and provide data to academic research.

REFERENCES

[1] R. T. Tsunoda, "High-latitude F-region irregularities: A review and synthesis," *Rev. Geophys.*, vol. 26, pp. 719–760, 1988.
[2] J. J. Makela, "A review of imaging low-latitude ionospheric irregularity processes," *J. Atmos. Sol. Terr. Phys.*, vol. 68, pp. 1441–1458, 2006.
[3] Y. Liu *et al.*, "Review of ionospheric irregularities and ionospheric electrodynamic coupling in the middle latitude region," *Earth Planet. Phys.*, vol. 5, pp. 462–482, 2021.
[4] B. G. Fejer and M. Kelley, "Ionospheric irregularities," *Rev. Geophys.*, vol. 18, pp. 401–454, 1980.
[5] M. C. Kelley, *The Earth's Ionosphere: Plasma Physics and Electrodynamics*. New York, NY, USA: Academic, 2009.
[6] D. Bilitza *et al.*, "International reference ionosphere 2016: From ionospheric climate to real-time weather predictions," *Space Weather*, vol. 15, pp. 418–429, 2017.
[7] Y. Jin *et al.*, "Ionospheric plasma irregularities characterized by the Swarm satellites: Statistics at high latitudes," *J. Geophys. Res. Space Phys.*, vol. 124, pp. 1262–1282, 2019.
[8] A. Pignalberi, "TITIPy: A python tool for the calculation and mapping of topside ionosphere turbulence indices," *Comput. Geosci.*, vol. 148, 2021, Art. no. 104675.
[9] A. Pignalberi *et al.*, "A new ionospheric index to investigate electron temperature small-scale variations in the topside ionosphere," *Universe*, vol. 7, 2021, Art. no. 290.
[10] I. Cherniak, I. Zakharenkova, and R. J. Redmon, "Dynamics of the high-latitude ionospheric irregularities during the 17 March 2015 St. Patrick's day storm: Ground-based GPS measurements," *Space Weather*, vol. 13, pp. 585–597, 2015.
[11] I. Cherniak and I. Zakharenkova, "High-latitude ionospheric irregularities: Differences between ground- and space-based GPS measurements during the 2015 St. Patrick's day storm," *Earth, Planets Space*, vol. 68, 2016, Art. no. 136.
[12] P. De Michelis *et al.*, "On the 2015 St. Patrick storm turbulent state of the ionosphere: Hints from the swarm mission," *J. Geophys. Res. Space Phys.*, vol. 125, 2020, Art. no. e27934.
[13] P. De Michelis *et al.*, "Looking for a proxy of the ionospheric turbulence with Swarm data," *Sci. Rep.*, vol. 11, 2021, Art. no. 6183.
[14] I. Zakharenkova, E. Astafyeva, and I. Cherniak, "GPS and in situ Swarm observations of the equatorial plasma density irregularities in the topside ionosphere," *Earth, Planets Space*, vol. 68, 2016, Art. no. 120.
[15] M. Piersanti *et al.*, "From the Sun to Earth: Effects of the 25 August 2018 geomagnetic storm," *Ann. Geophys.*, vol. 38, pp. 703–724, 2020.
[16] P. De Michelis *et al.*, "Ionospheric turbulence and the equatorial plasma density irregularities: Scaling features and RODI," *Remote Sens.*, vol. 13, 2021, Art. no. 759.
[17] X. H. Shen *et al.*, "The state-of-the-art of the China seismo-electromagnetic satellite mission," *Sci. China Technological Sci.*, vol. 61, pp. 634–642, 2018.
[18] E. Friis-Christensen, H. Lühr, and G. Hulot, "Swarm: A constellation to study the Earth's magnetic field," *Earth, Planets Space*, vol. 58, pp. 351–358, 2006.
[19] M. Pezzopane *et al.*, "Occurrence of GPS loss of lock based on a Swarm half-solar cycle dataset and its relation to the background ionosphere," *Remote Sens.*, vol. 13, 2021, Art. no. 2209.
[20] X. Wang, W. Cheng, D. Yang, and D. Liu, "Preliminary validation of in situ electron density measurements onboard CSES using observations from Swarm satellites," *Adv. Space Res.*, vol. 64, pp. 982–994, 2019.
[21] R. Yan *et al.*, "Comparison of electron density and temperature from the CSES satellite with other space-borne and ground-based observations," *J. Geophys. Res. Space Phys.*, vol. 125, 2020, Art. no. e27747.
[22] J. Liu, Y. Guan, X. Zhang, and X. Shen, "The data comparison of electron density between CSES and DEMETER satellite, Swarm constellation and IRI model," *Earth Space Sci.,* vol. 8, 2021, Art. no. e2020EA001475.
[23] R. Yan *et al.*, "The langmuir probe onboard CSES: Data inversion analysis method and first results," *Earth Planet. Phys.*, vol. 2, pp. 479–488, 2018.
[24] C. Liu *et al.*, "The technology of space plasma in-situ measurement on the China seismo-electromagnetic satellite," *Sci. China Technol. Sci.*, vol. 62, pp. 829–838, 2019.
[25] M. B. Wilk and R. Gnanadesikan, "Probability plotting methods for the analysis for the analysis of data," *Biometrika*, vol. 55, pp. 1–17, 1968.
[26] M. Li *et al.*, "Primary joint statistical seismic influence on ionospheric parameters recorded by the CSES and DEMETER satellites," *J. Geophys. Res. Space Phys.*, vol. 125, 2020, Art. no. e28116.
[27] T. J. Immel *et al.*, "Control of equatorial ionospheric morphology by atmospheric tides," *Geophys. Res. Lett.*, vol. 33, 2006, Art. no. L15108.
[28] H. Lühr, K. Häusler, and C. Stolle, "Longitudinal variation of F region electron density and thermospheric zonal wind caused by atmospheric tides," *Geophys. Res. Lett.*, vol. 34, 2007, Art. no. L16102.
[29] L. Scherliess, D. C. Thompson, and R. W. Schunk, "Longitudinal variability of low-latitude total electron content: Tidal influences," *J. Geophys. Res.*, vol. 113, 2008, Art. no. A01311.

[1] [Online]. Available: http://cses.roma2.infn.it
[2] [Online]. Available: https://www.leos.ac.cn/

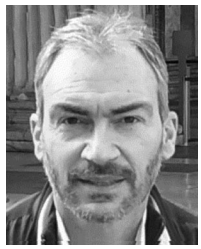

Michael Pezzopane received the M.Sc. degree in physics from the Sapienza University of Rome, Rome, Italy, in 1997, and the Ph.D. degree in geophysics from the Alma Mater Studiorum University of Bologna, Bologna, Italy, in 2005.

Since 2001, he has been a Geophysicist with the Upper Atmosphere Physics and Radiopropagation Unit, Istituto Nazionale di Geofisica e Vulcanologia, Rome, Italy. He has authored or coauthored more than 100 papers published in scientific peer-reviewed journals. His main research interests include ionospheric physics, radio wave propagation in the ionosphere, atmospheric gravity waves, autoscaling of vertical ionospheric soundings, electron density irregularities at low latitudes, the E sporadic layer, topside modeling, and three-dimensional electron density modeling of the ionosphere.

Dr. Pezzopane is a Topical Editor for *Annals of Geophysics* and a member of the International Reference Ionosphere Working Group.

Alessio Pignalberi received the B.S. and M.S. degrees in physics from the Sapienza University of Rome, Rome, Italy, in 2011 and 2014, respectively, and the Ph.D. degree in geophysics from the Alma Mater Studiorum University of Bologna, Bologna, Italy, in 2019.

He is currently a Postdoctoral Researcher with the Istituto Nazionale di Geofisica e Vulcanologia, Rome, Italy. His main research interests include the development, implementation, and validation of data-assimilation empirical ionospheric models, the modeling of the ionosphere topside electron density profile, the study of small-scale properties of ionospheric plasma through ionospheric indices, and the study of large-scale climatological properties of ionospheric plasma.

Paola De Michelis received the M.Sc. degree in physics from the La Sapienza University of Rome, Rome, Italy, in 1995, and the Ph.D. degree in polar sciences from the University of Siena, Siena, Italy, in 2012.

She is currently a Senior Research Scientist with Istituto Nazionale di Geofisica e Vulcanologia, Rome, Italy, in the field of geomagnetism and solar–terrestrial physics. Her research focuses on changes in the Earth's magnetic field that occur on time scales from minutes to millennia, exploring mainly observational aspects. One of her primary interests lies in space physics, with a focus on the dynamics of the Earth's magnetosphere, the processes due to the Sun–Earth interaction, and space weather phenomena. In particular, her studies are devoted to the emergence of nonlinear and complex dynamics in the Earth's processes in response to the solar wind changes using data recorded on the ground and in space. In recent years, she used the Earth's magnetic field fluctuations as well as electron density fluctuations recorded by the Swarm constellation to provide a multiparametric characterization of turbulence and complexity in the F-region of the ionosphere.

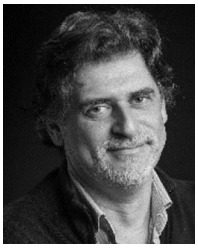

Giuseppe Consolini received the Laurea in physics from the La Sapienza University of Rome, Rome, Italy, in 1991, in the field of matter and quantum physics applied to biosystems.

Then, he moved to the field of Sun–Earth relationships, working on the complexity of the Earth's magnetospheric response to solar wind changes He is currently a Senior Research Scientist with the National Institute for Astrophysics, Rome, Italy, in the field of space physics and solar–terrestrial physics. He coauthored more than 200 publications in ISI-WOS indexed journals/reviews. His research interests include the complexity and turbulence in space plasmas and solar physics, with a special emphasis on the geospace plasma dynamics in the interplanetary medium and the magnetosphere–ionosphere system.

Dr. Consolini received the Dr. Giuseppe Borgia Foundation Award in 2000, assigned by the Accademia Nazionale dei Lincei, Italy, for his studies on the criticality of the Earth's magnetosphere during magnetospheric substorms.

Igino Coco received the graduate degree in physics from the University of Pavia, Pavia, Italy, in 2000, with an experimental thesis on the characterization of a sensor for the detection of buried explosives based on nuclear techniques, and the Ph.D. degree in polar sciences from the University of Siena, Siena, Italy, in 2005.

After his graduation, he completely changed his research topics and began to work on ionospheric physics and magnetosphere–ionosphere coupling, mainly by means of ground-based high-frequency radars (SuperDARN network). He was a Research Fellow with the Istituto di Fisica dello Spazio Interplanetario (now Istituto di Astrofisica e Planetologia Spaziali), Rome, Italy, which is part of the Istituto Nazionale di Astrofisica. In 2009, he was deputed by SuperDARN Italian Principal Investigator, Dr. Ermanno Amata, to the project management for the construction of the Italian SuperDARN radar Dome C East, at the Concordia station, in Antarctica. In 2012, he joined the ESA ground segment team of the Swarm mission, supervising the quality assessment of plasma data and coordinating the Electric Field Instrument Expert Group. Since December 2016, he has been a permanent researcher with the Istituto Nazionale di Geofisica e Vulcanologia, Rome, Italy. His main field of study is space weather, through the analysis of ionospheric parameters (electron density and temperature, plasma convection, and electric field) both *in situ* (satellite measurements) and from ground (coherent scatter radars), following impulsive changes in the interplanetary medium (e.g., shocks, geomagnetic storms, and ionospheric storms).

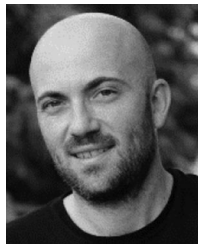

Fabio Giannattasio received the second-level master's degree in space science and technology and the Ph.D. degree in astrophysics from the University of Rome Tor Vergata, in 2021 and 2013, respectively.

From 2014 to 2016, he was a Postdoctoral Fellow with Osservatorio Astronomico di Roma and with the Institute for Space Astrophysics and Planetology, both part of the Istituto Nazionale di Astrofisica, where he worked on the spectropolarimetric observations of the solar atmosphere, the dynamic properties of solar magnetic field at small scales, and the Sun–Earth interactions. Since the end of 2016, he has been a Researcher with the Istituto Nazionale di Geofisica e Vulcanologia, Rome, Italy. His research activity focuses on the study of phenomena that are relevant to space weather: some aspects inherent to the physics of the solar atmosphere, the ionospheric turbulence, and the magnetosphere–ionosphere coupling.

Roberta Tozzi received the M.Sc. degree in physics from the Sapienza University of Rome, Rome, Italy, in 1999, and the Ph.D. degree in geophysics from the "Alma Mater Studiorum" University of Bologna, Bologna, Italy, in 2003.

Since 2003, she has been with the Unit of Geomagnetism, Istituto Nazionale di Geofisica e Vulcanologia, Rome, Italy. Her main research interests include geomagnetic field variations, of both internal (Earth interior) and external (magnetospheric and ionospheric) origins, implementation of mathematical methods for data (from both ground and satellite observations) exploitation, and ground effects of space weather events.

Simona Zoffoli received the graduate degree in physics from Università La Sapienza in Rome, Rome, Italy, in 1997, and the Ph.D. degree in geodesy and geomatics from Politecnico di Milano, Milan, Italy, in 2009.

Since 1998, she has been with the Italian Space Agency (ASI), Rome, Italy, where she is working on earth observation programs. As a Program Manager, she has managed several science and applications programs mainly focused on how Earth observation space data can support disaster risk management activities and environmental monitoring. During her career, she has also been involved in formulation studies of numerous Earth observation missions and payloads. She was the ASI Program Manager for the LIMADOU—CSES-01 mission that launched in 2018. She is currently the ASI Program Manager for the LIMADOU—CSES-02 mission. She is a delegate to the ESA DOSTAG and the former Chair of the CEOS Working Group on Disasters.